Tectonic strain causes the inclination divergence of paleomagnetic data from the Upper Cretaceous redbeds in the Lhasa terrane, insight from AMS, hf-AIR and CPO

Hongliang Lu[1,2], Qian Zhao[3], Zhiyu Yi[4], Baochun Huang[1], and Josep M. Parés[2]

[1]Key Laboratory of Orogenic Belt and Crustal Evolution, School of Earth and Space Sciences, Peking University
[2]CENIEH
[3]Department of Resources and Environmental Sciences, Quanzhou Normal University
[4]Sun Yat-sen University - Zhuhai Campus

September 26, 2024

Abstract

Paleomagnetic data from the Lhasa terrane have been commonly utilized to constrain the paleo-position and shape of the southern margin of Asia prior to the India-Asia collision. However, there has been an ongoing debate regarding the reliability of the paleomagnetic data derived from Cretaceous sedimentary rocks in the Lhasa terrane. Here, we employ combined anisotropy of magnetic susceptibility (AMS), high-field anisotropy of isothermal remanent magnetization (hf-AIR), and crystal preferred orientation (CPO) measurement on the redbeds of the Shexing Formation. Regardless of the structure displayed in the AMS data, the hf-AIR results demonstrate a weak cleavage to deformational magnetic fabric, with minimum axes corresponding roughly with the c-axis of hematite in the bedding plane. Consequently, we propose that the inclination divergence observed between the two limbs of an anticline in the Late Cretaceous paleomagnetic data from the Lhasa terrane is attributable to the deflection of hematite under weak post-depositional tectonic strain. We caution against using Upper Cretaceous redbeds from the Lhasa terrane for paleogeographic reconstruction without an efficient correction of tectonic strain. Furthermore, we suggest the adoption of anisotropy of magnetic remanence (AMR) as a more suitable alternative to AMS for assessing the reliability of paleomagnetic data in sedimentary rocks.

Tectonic strain causes the inclination divergence of paleomagnetic data from the Upper Cretaceous redbeds in the Lhasa terrane, insight from AMS, hf-AIR and CPO

Hongliang Lu[1,2], Qian Zhao[3], Zhiyu Yi[4,5], Baochun Huang[1], and Josep M. Parés[2]

[1]Key Laboratory of Orogenic Belts and Crustal Evolution, School of Earth and Space Sciences, Peking University, Beijing 100871, China.

[2]Geochronology, Research Center for Human Evolution (CENIEH), Burgos 09002, Spain.

[3]Department of Resources and Environmental Sciences, Quanzhou Normal University, Quanzhou 362000, China.

[4]Planetary Environment and Astrobiological Research Laboratory (PEARL), School of Atmospheric Sciences, Sun Yat-sen University, Zhuhai, China.

[5]Key Laboratory of Tropical Atmosphere-Ocean System, Ministry of Education, Zhuhai 519082, China.

Corresponding author: Baochun Huang (bchuang@pku.edu.cn)

Key Points:

- The inclination divergence originated from the deflection of hematite due to weak post-depositional deformation.
- The "syntectonic-sedimentation-correction" proposed by Tong et al. (2019) was based on an error in growth strata bedding correction.
- AMR, rather than AMS, could be a better indicator of whether paleomagnetic data has been affected by tectonic strain.

Abstract

Paleomagnetic data from the Lhasa terrane have been commonly utilized to constrain the paleo-position and shape of the southern margin of Asia prior to the India-Asia collision. However, there has been an ongoing debate regarding the reliability of the paleomagnetic data derived from Cretaceous sedimentary rocks in the Lhasa terrane. Here, we employ combined anisotropy of magnetic susceptibility (AMS), high-field anisotropy of isothermal remanent magnetization (hf-AIR), and crystal preferred orientation (CPO) measurement on the redbeds of the Shexing Formation. Regardless of the structure displayed in the AMS data, the hf-AIR results demonstrate a weak cleavage to deformational magnetic fabric, with minimum axes corresponding roughly with the c-axis of hematite in the bedding plane. Consequently, we propose that the inclination divergence observed between the two limbs of an anticline in the Late Cretaceous paleomagnetic data from the Lhasa terrane is attributable to the deflection of hematite under weak post-depositional tectonic strain. We caution against using Upper Cretaceous redbeds from the Lhasa terrane for paleogeographic reconstruction without an efficient correction of tectonic strain. Furthermore, we suggest the adoption of anisotropy of magnetic remanence (AMR) as a more suitable alternative to AMS for assessing the reliability of paleomagnetic data in sedimentary rocks.

Plain Language Summary

Scientists have been using paleomagnetic studies of the Lhasa terrane to determine where the southern edge of Asia was before it collided with India. But, there's been a lot of discussion about whether we can trust what these studies conclude about the Cretaceous redbeds from this area, because of the huge discrepancy among different paleomagnetic studies. In our research, we looked at the magnetic properties of the redbeds from the Shexing Formation with three different methods. Even if the results from anisotropy of magnetic susceptibility (AMS) seemed to show different patterns, our findings using high-field anisotropy of isothermal remanent magnetization (hf-AIR) suggested that the rocks were affected by tectonic strain, showing changes aligning with crystal preferred orientation (CPO) of hematite in the rocks. This leads us to believe that the changes we see in the rocks' magnetic directions come from the

tectonic forces. Consequently, we recommend being very careful about using data from the redbeds of the Shexing Formation to figure out paleogeography unless we understand how the redbeds have been deformed over time. We also think anisotropy of magnetic remanence (AMR) might be better for checking the reliability of paleomagnetic studies in sedimentary rocks.

1 Introduction

The Cenozoic collision between India and Asia gave rise to the Himalayan Orogen, the largest orogenic belt globally, leading to the closure of the Neo-Tethys Ocean, potential crustal shortening across both tectonic plates, and extensive structural deformation within the Indus-Yarlung Tsangpo Suture Zone, from a global to a local perspective. The Lhasa terrane was once considered the southern margin of the Eurasian Plate before its collision with the Indian Plate (Yin & Harrison, 2000), and its Late Cretaceous paleomagnetic results have been widely used to constrain the paleolatitude and shape of this pioneer terrane (Bian et al., 2020; Cao et al., 2017; Liang et al., 2017; Ma et al., 2022; Ma et al., 2017; Sun et al., 2012; Tan et al., 2010; Tong et al., 2019; Tong et al., 2017; Yang et al., 2019; Yang et al., 2015; Yi et al., 2015; Zhao et al., 2021), which is critical to pinpointing the collision's timing and quantifying the Eurasian continent's crustal shortening. Nevertheless, despite extensive geological and geophysical research on the Lhasa terrane, its precise Late Cretaceous paleogeographic position remains a topic of debate (Jadoon et al., 2024).

Recent paleomagnetic studies on the Shexing Formation redbeds have yielded a range of paleolatitudes from ~10°N to ~24°N within the central and eastern sectors of the Lhasa terrane (Cao et al., 2017; Ma et al., 2022; Sun et al., 2012; Tan et al., 2010; Tong et al., 2017). A primary issue under debate is the extent of inclination shallowing effect in the Late Cretaceous redbeds from the Linzhou Basin: while some researchers have implemented inclination corrections using elongation/inclination (E/I) analysis (Tan et al., 2010), others dispute the presence of significant inclination shallowing (Cao et al., 2017; Sun et al., 2012; Tong et al., 2017). More crucially, many studies (Bian et al., 2020; Cao et al., 2017; Li et al., 2016; Ma et al., 2014; Sun et al., 2012; Tan et al., 2010; Tong et al., 2019; Tong et al., 2017; Wang et al., 2022; Yang et al., 2015) reported "syn-folding" fold test results (Figure 1c) from the Lhasa terrane redbeds, which are typically characterized by shallower inclinations on the northern limb of an anticline and steeper inclinations on the southern limb after tilt correction (Figures 1a and 1b, Table 1, see more detailed summary in Tong et al., 2019). According to these "syn-folding" results, combined with the deformed fabric in anisotropy of magnetic susceptibility (AMS) measurements and the identification of secondary hematite in petrological investigation, Liang et al. (2017) proposed that the Linzhou Basin Shexing Formation redbeds underwent remagnetization.

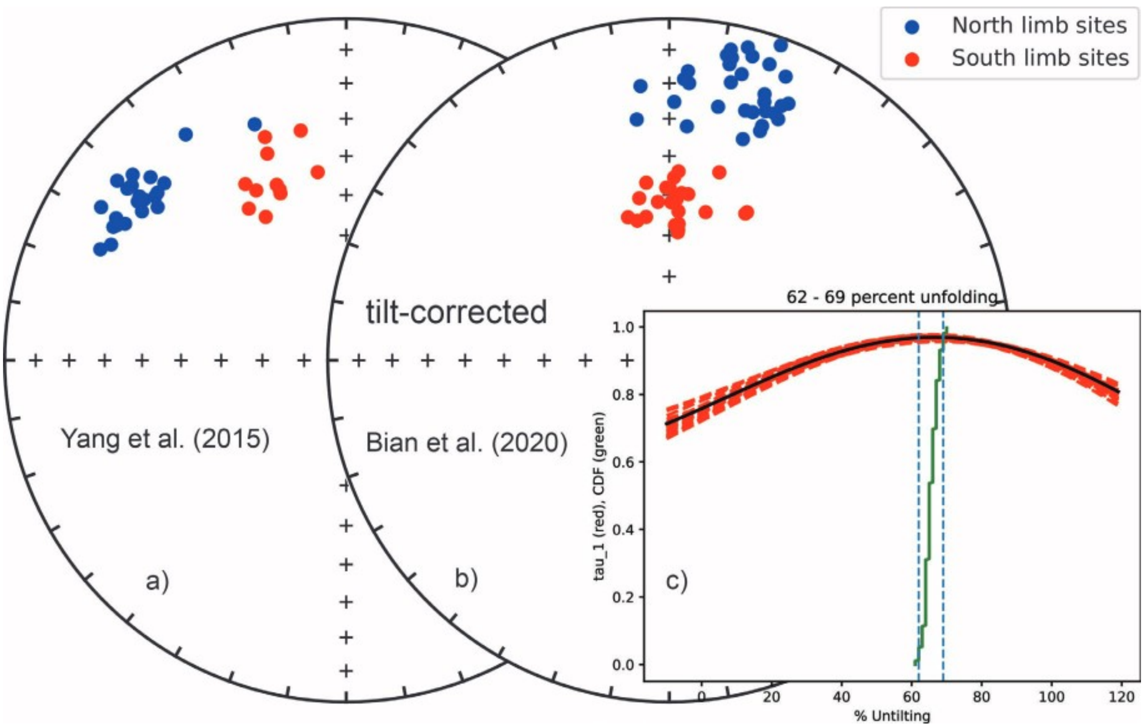

Figure 1. Two examples of the inclination divergence of the Late Cretaceous redbeds from the Lhasa terrane. The equal-area projection of the paleomagnetic directions from the two limbs in (a) Yang et al. (2015) and (b) Bian et al. (2020). (c) The fold test (Tauxe & Watson, 1994) result of Bian et al. (2020), produced by *Pmagpy* (Tauxe et al., 2016). CDF: cumulative distribution function.

However, Tong et al. (2019) posited that the markedly different inclinations noted on each fold limb result from syn-depositional growth strata, thus the characteristic remanent magnetization (ChRM) directions are reliable after the identification and correction of growth strata (Bian & Yang, 2021; Bian et al., 2020; Ma et al., 2023; Sun et al., 2023; Wang et al., 2022), although they didn't have any field evidence for the existence of the growth strata. In contrast, Zhao et al. (2021) argued that the inclination difference arises from post-depositional tectonic strain during the folding process (Kodama, 1988). According to these authors, the paleomagnetic directions, as recorded by the carrier mineral, undergoes rotation in two distinct directions, resulting in one limb exhibiting a steeper inclination and the other a shallower one after the tilt correction. We will discuss these two models in detail in section 5.1.

These two conflicting hypotheses regarding the primariness of the redbeds paleomagnetic direction yield distinct predictions for the anisotropy of remanent magnetization and the crystal-preferred orientation (CPO) of hematite within the redbeds, assuming hematite is the only remanent magnetization carrier. Under the growth strata model, the magnetic fabric is expected to exhibit a sedimentary fabric, with the *K*min axis predominantly perpendicular to the bedding plane (Hrouda & Chadima, 2019), or slightly tilted in accordance with the growth strata angle (Sun et al., 2023). Likewise, the c-axis of hematite, as determined by electron backscatter diffraction (EBSD) is also expected to be perpendicular to the bedding plane (Biedermann, 2018). Conversely, the tectonic strain model implies a deformational magnetic fabric, with the *K*min axis deviating from being perpendicular to the bedding plane, exhibiting dispersion or convergence in different directions (Hrouda & Chadima, 2019), which affects the orientation of hematite's c-axis as well. This divergence in the anisotropy of remanent magnetization and CPO can serve as a key discriminator in distinguishing between syn-depositional growth strata effects and post-depositional tectonic strain on the Upper Cretaceous redbeds from the Lhasa terrane.

To advance our comprehension of the remanence-carrying ferromagnetic minerals in the Late Cretaceous redbeds of the Lhasa terrane and to address the ongoing debate between growth strata and tectonic strain interpretations, besides the AMS, which is commonly and rapidly measured in paleomagnetic study and represents the susceptibility contribution from all minerals, we also analyzed the high-field anisotropy of isothermal remanent magnetization (hf-

AIR, a type of anisotropy of magnetic remanence, AMR), and the CPO of hematite within the Shexing Formation redbeds from the Linzhou Basin and Maxiang area. This comprehensive approach aims to shed light on the state of ferromagnetic minerals within the orogen, contributing valuable insights into the geological processes affecting the paleomagnetic directions observed in these regions. Our results show that the sedimentary hematite in the central-eastern Lhasa terrane has undergone deflections due to tectonic strain, casting doubts on the reliability of paleomagnetic data from these redbeds for use in paleogeographic reconstructions.

2 Geological setting and Sampling

The Lhasa terrane is located between the Indus-Yarlung Tsangpo Suture Zone and the Bangong-Nujiang Suture Zone, with the Qiangtang terrane to the north and the Tethyan-Himalaya to the south (Figure 2a). During the Late Jurassic-Early Cretaceous, the Lhasa terrane merged with the Qiangtang terrane in southern Asia prior to colliding with India (Li et al., 2016).

On the Lhasa terrane, the Ordovician and Carboniferous-Triassic shallow marine sediments overlie the crystalline basement of the Middle Proterozoic-Early Cambrian, followed by Late Jurassic-Early Cretaceous marine succession unconformably covering this shallow marine sedimentary unit. Beginning from the mid-Cretaceous, the strata evolved from marine to terrestrial, with the Upper Cretaceous being the continental redbeds (He et al., 2007; Tapponnier et al., 1981; Yin & Harrison, 2000). Additionally, the Gangdise batholith is present in the southern part of the Lhasa terrane, formed by Andean-type subduction from 95 Ma to 38 Ma as India moved northward relative to Eurasia (Allegre et al., 1984; Yin & Harrison, 2000). In Late Cretaceous to Paleocene, there is a significant disparity in deformation between the tightly folded Precambrian to Mesozoic rocks and the mildly folded and faulted Paleocene and Eocene volcanic and volcaniclastic sediments of the Linzizong Group (Tapponnier et al., 1981). The Linzizong volcanism is contemporaneous with and genetically related to, the Gangdise batholith

(Yin & Harrison, 2000). The Cretaceous-Tertiary unconformity is commonly interpreted as denoting the onset of the India-Asia collision (Mo et al., 2003).

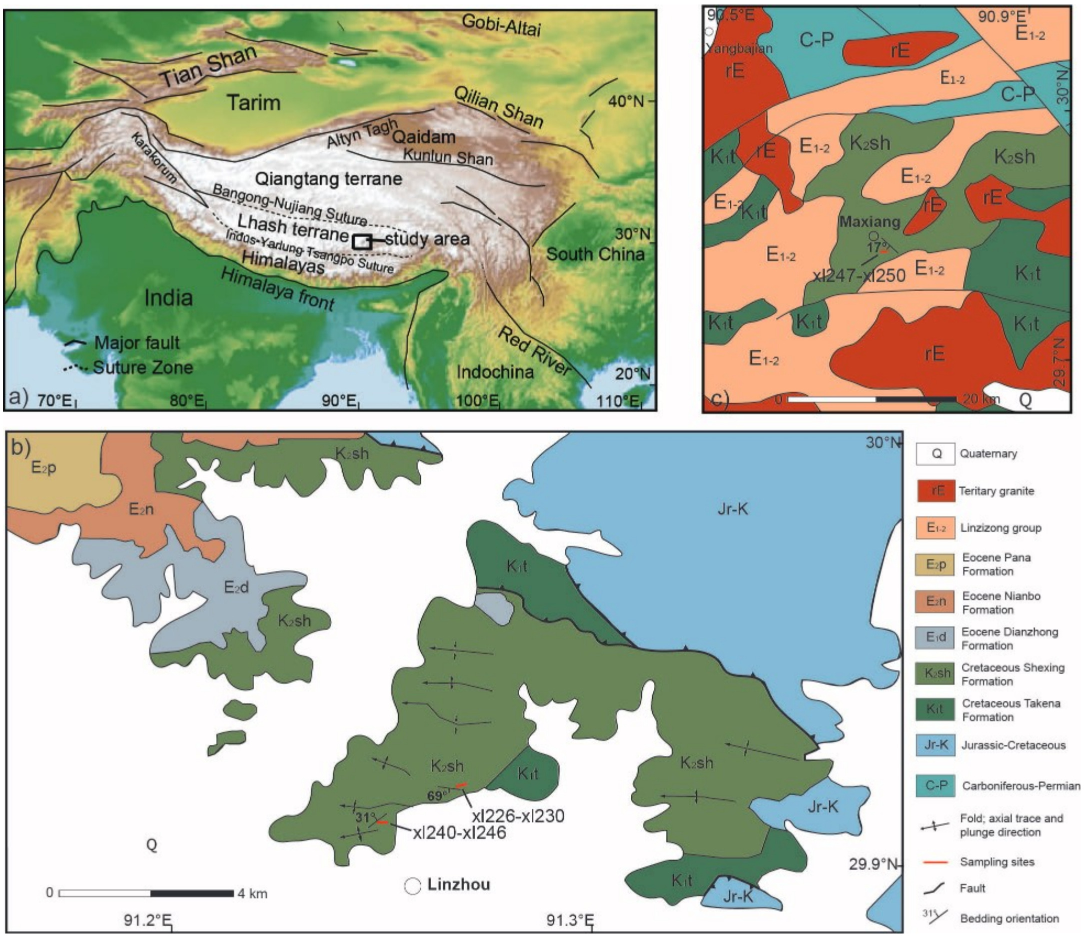

Figure 2. Geological map of Tibet and the investigation area. (a) Simplified tectonic map of Tibet Plateau, showing the main blocks, sutures, and faults (modified from Sun et al.,2012). (b) Geologic map of the Linzhou Basin, Lhasa (modified from He et al., 2007) and positions of two sampling sections. (c) Geologic map of the Maxiang area, Lhasa (modified from Sun et al., 2012) and position of one sampling section.

In the Linzhou Basin (~ 60 km northeast of Lhasa, Figure 2b) and the Maxiang area (~ 80 km northwest of Lhasa, Figure 2c), the Upper Cretaceous Shexing Formation redbeds interbedded with andesite lava are exposed, overlying the Lower Cretaceous Takena Formation and being unconformably overlain by the Early Tertiary volcanic strata of the Linzizong Group. Previous researchers have conducted a significant amount of paleomagnetic research in these strata (Bian et al., 2020; Cao et al., 2017; Liang et al., 2017; Ma et al., 2022; Sun et al., 2012; Tan et al., 2010; Tong et al., 2019; Zhao et al., 2021). To more directly verify the reliability of these results, we selected three sampling sections same as previous studies: 1) the xl240-xl246 sites on the north limb of the Shexing anticline (average bedding dip direction=323°, dip=31°), which is the same as the xl210-xl215 sites in Liang et al. (2017); 2) the xl226-xl230 sites at the same layers as section B in Tan et al. (2010) (average bedding dip direction=187°, dip=69°), including the controversial "lava flow" layers from site xl227; 3) the xl247-xl250 sites in the Maxiang area (average bedding dip direction=222°, dip=17°), which is the same redbeds as that sampled by Sun et al. (2012). At each site, 6-12 cores with a diameter of 2.5 cm were collected using a gasoline-powered drill and oriented with both magnetic and Sun compasses. Detailed sample number, site GPS and bedding orientation can be found in Table S1 in Supporting Information S1. No evidence of growth strata was reported in these areas.

To study the remanence-carrying magnetic minerals within these redbeds, Liang et al. (2017) conducted a Raman spectroscopic analysis which revealed that metallic minerals in the thin section were predominantly composed of hematite, with minor quantities of magnetite. However, they also found that pseudomorphic hematite often filled the interstitial spaces between quartz particles, while grid-like hematite displayed signs of intricate deformation history. In Tan et al. (2010) and Sun et al. (2012), only the high unblocking temperature (up to 680°C) indicates the presence of hematite.

In the laboratory, rock cores were processed into standard-sized samples with a length of 2.2 cm for AMS measurements. For hf-AIR analyses, smaller samples were prepared using a tabletop drill to extract cores with a 9 mm diameter, which were then sectioned into cylinders 7 mm in length to fit the smallest coil of the impulse magnetizer. These small cylinders were oriented as same as the standard-sized samples to ensure consistency. Standard-sized plastic cylinder molds were produced to contain the small samples during the magnetization measurement. For oriented EBSD analysis, resin-embedded thin sections with a thickness of 0.03 mm were produced parallel to the top and bottom surfaces of the paleomagnetic cylinder samples. These thin sections were oriented such that the z-axis of the cylinder samples was perpendicular to the thin section's exterior surface, and the x-axis was parallel to the longer edge of the thin section.

3 Methods

AMS is typically used as a key indicator of the tectonic deformation experienced by rocks (Hrouda & Chadima, 2019; Parés, 2004, 2015). However, there is a noticeable absence of AMS data in certain studies (Tan et al., 2010; Tong et al., 2017), while others, such as Sun et al. (2012) and Liang et al. (2017), have reported diverse AMS fabric types from identical geological sections. Moreover, Ma et al. (2022) neglected the deformational AMS fabric based on the consistent ChRM inclination with Cao et al. (2017), where the AMS shows sedimentary-pencil structure fabric. Therefore, AMS data for the Shexing Formation redbeds in the Linzhou Basin and Maxiang region require thorough and careful assessment. The new AMS measurements presented in this study were conducted using the Agico Kappabridge MFK1.

Given that AMS at low-field and room-temperature evaluate the magnetic susceptibility anisotropy of all mineral components within a rock sample, it is imperative to scrutinize the fabric of remanence-carrying ferromagnetic minerals specifically, because sometimes the AMS fabric carried by paramagnetic minerals could be different from the AMR carried by ferromagnetic minerals (Hrouda et al., 2018). High coercivity hematite has been identified as the remanence carrier within the Shexing Formation (Liang et al., 2017; Sun et al., 2012; Tan et al., 2010). Therefore, we employed the hf-AIR technique proposed by Bilardello and Kodama (2009) to analyze the hematite texture. The technique involves: 1) activating hematite to saturation magnetization with a 5T pulse DC field produced by ASC IM-10-30 impulse magnetizer, 2) conducting a 100 mT alternating field demagnetization in three axes with a D2000 alternating field demagnetizer to eliminate the remanence of ferromagnetic minerals with coercivity lower than 100 mT (such as magnetite or maghemite), 3) conducting a 150°C thermal demagnetization with a TD-48 oven to eliminate the remanence of ferromagnetic minerals with unblocking temperature lower than 150 mT (such as goethite), 4) measuring the remanent magnetization within the standard-cylinder-sample-size plastic mould in a AGICO JR6 spinner magnetometer, 5) repeating steps 1-4 in nine orientations (x, y, z, xy, xz, yz, -xy, -xz and -yz), 6) calculating the 6 parameters of the hf-AIR tensor from the 9-direction measurement (Girdler, 1961), 7) calculating the 3 principal axes orientation and eigenvalues of the hf-AIR tensor and conducting the geographic and stratigraphic coordinate correction. These magnetic experiments were conducted at the Magnetotectonics Laboratory, School of Earth and Space Sciences, Peking University, with statistical analyses (bootstrap of anisotropy tensor and cumulative distribution of eigenvalues) and figure production facilitated by *PmagPy* (Tauxe et al., 2016).

While hf-AIR effectively minimizes interference from certain minerals, pigmentary hematite, characterized by a wide coercivity spectrum and high unblocking temperature, may still affect hf-AIR outcomes (Bilardello, 2015). To precisely assess the CPO of detrital hematite, EBSD techniques were employed, conducted with the Oxford Instruments Aztec EBSD system at the SEM-EBSD laboratory, School of Earth and Space Sciences, Peking University. Before the experiment, the surface of the thin sections is subjected to fine polishing. The examination comprised mapping sections of samples with step sizes between 10 and 13 μm in a ~15 mm^2 area of the thin sections from xl240-xl246 samples and performing targeted point analyses on selected hematite grains from xl226-xl230 and xl247-xl250 samples, in which for each grain, 1 to 2 points were analyzed to capture its orientation accurately and a minimum of 200 (mostly > 250) data points were collected per specimen, providing a statistically robust dataset for analysis. *Channel5* software facilitated the data interpretation, producing CPO pole figures, in which the x,y, and z axes are consistent with the orientation system of paleomagnetic samples but with different projection methods in the original format. Then the figures were converted to the conventional x-to-up, y-to-right, lower-hemisphere projection utilized in paleomagnetic studies. The clustering points from these figures were then extracted and underwent coordinate correction from specimen coordinates to stratigraphic coordinates. Given that hematite is a monoclinic antiferromagnetic mineral with magnetization predominantly within the basal plane (Dunlop & Özdemir, 1997), its [001] axis (or c-axis) is hypothesized to align with the minimum axes of magnetic susceptibility and remanence (Biedermann, 2018).

4 Results

4.1 xl240-xl246 from the North Limb in Liang et al. (2017)

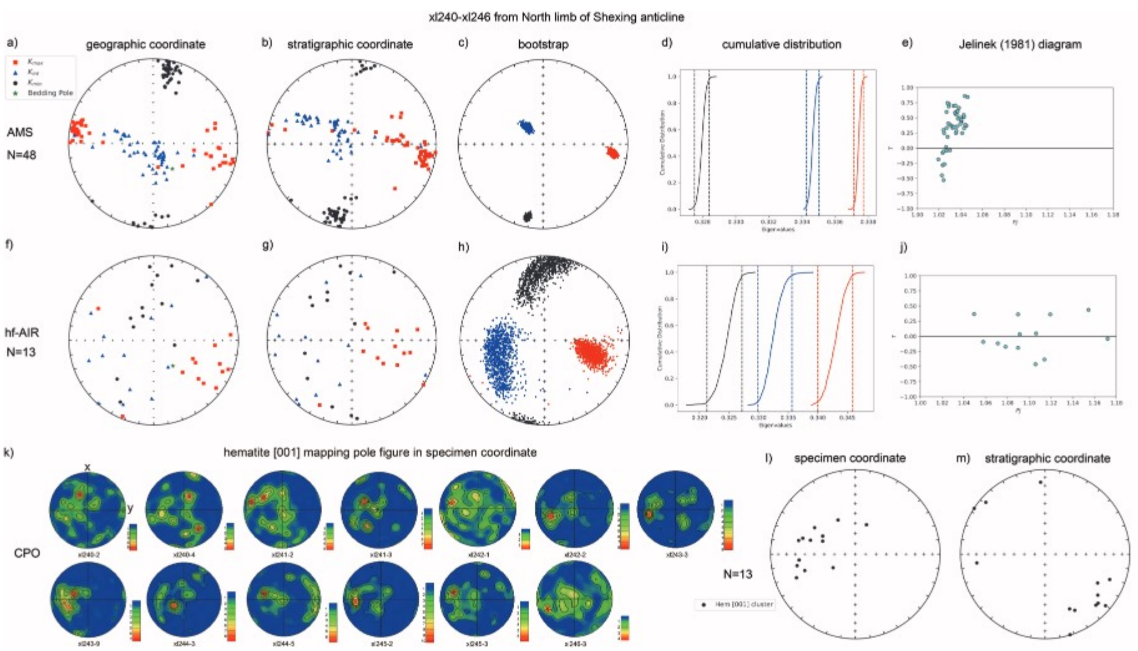

Figure 3. AMS, hf-AIR and CPO of hematite results of xl240-xl246 sites. (a-e) AMS results equal-area lower hemisphere projection in geographic coordinates and stratigraphic coordinates (with bootstrap results), the cumulative distribution of the bootstrap eigenvalues and Jelinek (1981) corrected anisotropy degree (Pj) versus ellipsoid shape factor (T) diagram (Pj-T). (f-j) hf-AIR results equal-area lower hemisphere projection in geographic coordinates and stratigraphic coordinates (with bootstrap results), the cumulative distribution of the bootstrap eigenvalues and Pj-T diagram. (k) Mapping pole figure of hematite [001] pole in equal-area lower hemisphere projection of specimen coordinates. (l and m) Equal-area lower hemisphere projection of the cluster directions of hematite [001] pole in specimen coordinates and stratigraphic coordinates.

The AMS results for samples from sites xl240-xl246 (Figures 3a-3c, raw data in Data Set S1), as already partially reported in Jia et al. (2023), displayed a tectonic fabric with *K*min near the bedding plane. The eigenvalue cumulative distribution (Figure 3d) and corrected anisotropy degree (Pj) versus ellipsoid shape factor (T) diagram (Pj-T, Figure 3e) reveal a dominant oblate ellipsoid. This finding is consistent with the AMS results in Fig. 6(a) of Liang et al. (2017), given the samples come from similar, though not identical, sites in the north limb of the Shexing anticline.

The hf-AIR for 13 samples from sites xl240-xl246 presented a similar albeit more scattered distribution (Figures 3f-3h, raw data in Data Set S1). *K*min remains close to the bedding plane, indicating a tectonic fabric. The scattered distribution of eigenvectors necessitated a verification of the ellipsoid's shape through a cumulative distribution plot and Pj-T plot (Figures 3i and 3j), confirming three distinct eigenaxes within the 95% confidence interval and higher anisotropy degree than AMS. The difference between hf-AIR and AMS is likely due to the different contributions of minerals, a topic to be explored in section 5.2. The scatter in hf-AIR eigenvectors could be attributed to the limited sample number or the influence of secondary hematite, which remains despite attempts to mitigate the effects of goethite and magnetite (Bilardello, 2015).

The mapping EBSD, firstly, confirmed that the highlight metallic minerals under the second electron microscope (SEM) photos are mainly hematite with minor quantity of magnetite (Figure S1 in Supporting Information S1, all the SEM photos and EBSD detected mineral distribution in Data Set S1). Secondly, it revealed a predominant orientation cluster of detrital hematite [001] poles (Figure 3k). The raw .cpr files and pole figures produced by *Channel5* can be found in Data Set S1, same for the next two sections. By extracting these cluster points (Figure 3l) and transferring them into stratigraphic coordinates (Figure 3m), the hematite [001] axis orientation was also found to be close to the bedding plane, akin to the *K*min of AMS and hf-AIR, yet not perfectly aligned, indicating a clear deflection of the hematite.

4.2 xl226-xl230 from Section B of Tan et al. (2010)

Given the geographic closeness of xl226-xl230 and xl240-xl246 sites (Figure 2b), one might expect to observe similar tectonic AMS and hf-AIR fabrics. However, the AMS data from xl226-xl230 (except the "lava-flow" site xl227) exhibited a pristine sedimentary fabric (Figures 4a-4c, raw data in Data Set S1), with an oblate ellipsoid (Figures 4d and 4e), typically deemed ideal for paleomagnetic studies. On the other hand, the AMS data of xl227 shows a deformational fabric (Figure 4f).

The hf-AIR results of xl226-xl230 (excluding xl227) displayed a more scattered orientation, with *K*min also deflecting from the vertical direction in stratigraphic coordinates (Figures 4g-4i, raw data in Data Set S1), which shows a tectonic fabric imprint. The cumulative distribution (Figure 4j) illustrated a broad dispersion of *K*min and *K*max values, but the anisotropy degrees (Figure 4k) were still higher than the AMS. To exclude the possibility that the scattered hf-AIR resulted from the unsaturation of the hematite in the hf-AIR measurement, we conducted the IRM acquisition curve (Figure 4l), which indicates the fully saturated hematite under a 5T field.

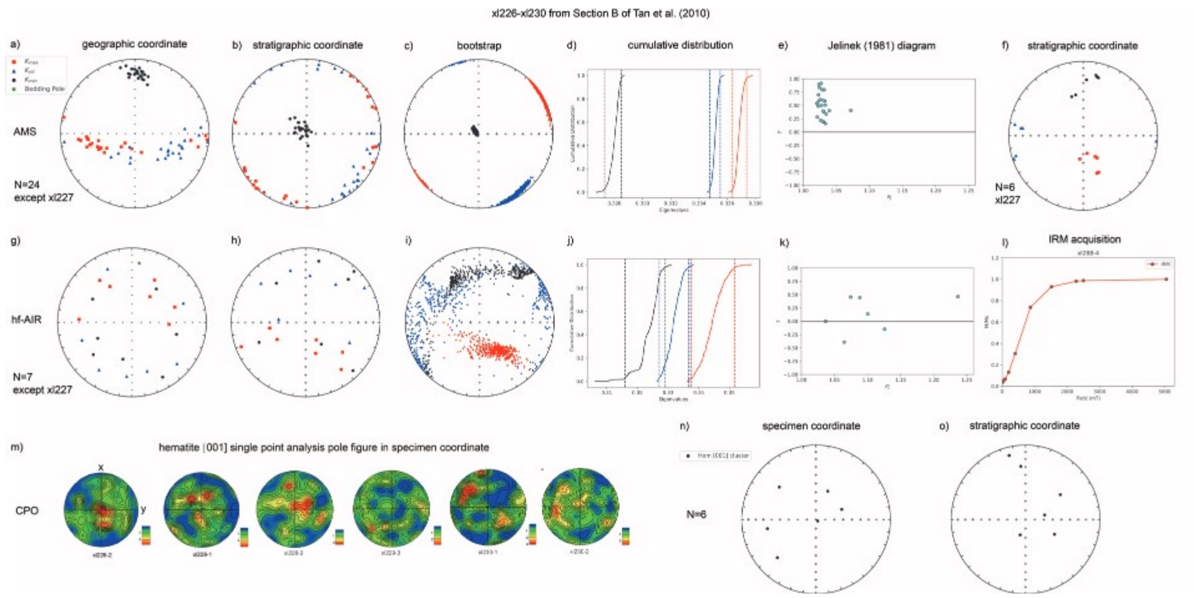

Figure 4. AMS, hf-AIR and CPO of hematite results of xl226-xl230 sites. (a-e) AMS results (excluding the xl227 site) equal-area lower hemisphere projection in geographic coordinates and stratigraphic coordinates (with bootstrap results), the cumulative distribution of the bootstrap eigenvalues and Jelinek (1981) corrected anisotropy degree (Pj) versus ellipsoid shape factor (T) diagram (Pj-T). (f) Equal-area lower hemisphere projection of xl227 AMS data in stratigraphic coordinate. (g-k) hf-AIR results (excluding the xl227 site) equal-area lower hemisphere projection in geographic coordinates and stratigraphic coordinates (with bootstrap results), the cumulative distribution of the bootstrap eigenvalues and Pj-T diagram. (l) IRM

acquisition curve of xl228-4. (m) Mapping pole figure of hematite [001] pole in equal-area lower hemisphere projection of specimen coordinates. (n and o) Equal-area lower hemisphere projection of the cluster directions of hematite [001] pole in specimen coordinates and stratigraphic coordinates.

In the EBSD single-point analysis of hematite, including at least 200 points per specimen for a pole figure (detailed point position photos for every specimen can be found in Data Set S1, same for the next section), it was observed that the [001] pole (Figure 4m) was less clustered than those in the mapping analysis of xl240-xl246 (Figure 3k). This difference arises because each hematite grain is given similar weight in the point analysis regardless of the grain's size, whereas, in the equal-step mapping analysis, larger hematite grains contribute more data points to the final results. Despite this, it is still possible to extract the most clustered directions from these pole figures (Figure 4n). However, these directions, when plotted in stratigraphic coordinates, are also dispersed (Figure 4o) and do not cluster vertically or within the bedding plane, indicating they cannot represent a "sedimentary fabric" in the conventional sense.

4.3 xl247-xl250 from the section of Maxiang area in Sun et al. (2012)

The AMS results for sites xl247-xl250 (Figures 5a-5c, raw data in Data Set S1), as already reported in Fig. 6e by Liang et al. (2017), depicted a tectonic fabric, diverging from the initial sedimentary fabric identified by Sun et al. (2012). The anisotropy ellipsoid presented is dominantly oblate (Figures 5d and 5e), with both eigenvalues and eigenvectors similar to those seen in sites xl240-xl246 (Figures 3b-3e).

Notably, a closer alignment between AMS and hf-AIR results (Figures 5f-5h, raw data in Data Set S1) was observed here, with both techniques indicating a tectonic fabric and similar orientations for eigenvectors. The hf-AIR data demonstrate a higher level of concentration compared to the previous two sections, displaying a typically oblate ellipsoid (Figures 5i and 5j) vertically oriented within the stratigraphic coordinates. The discrepancy between the eigenvalues of the maximum and intermediate axes was indistinguishable at the 95% confidence interval, yet there was a pronounced difference for the minimum axis.

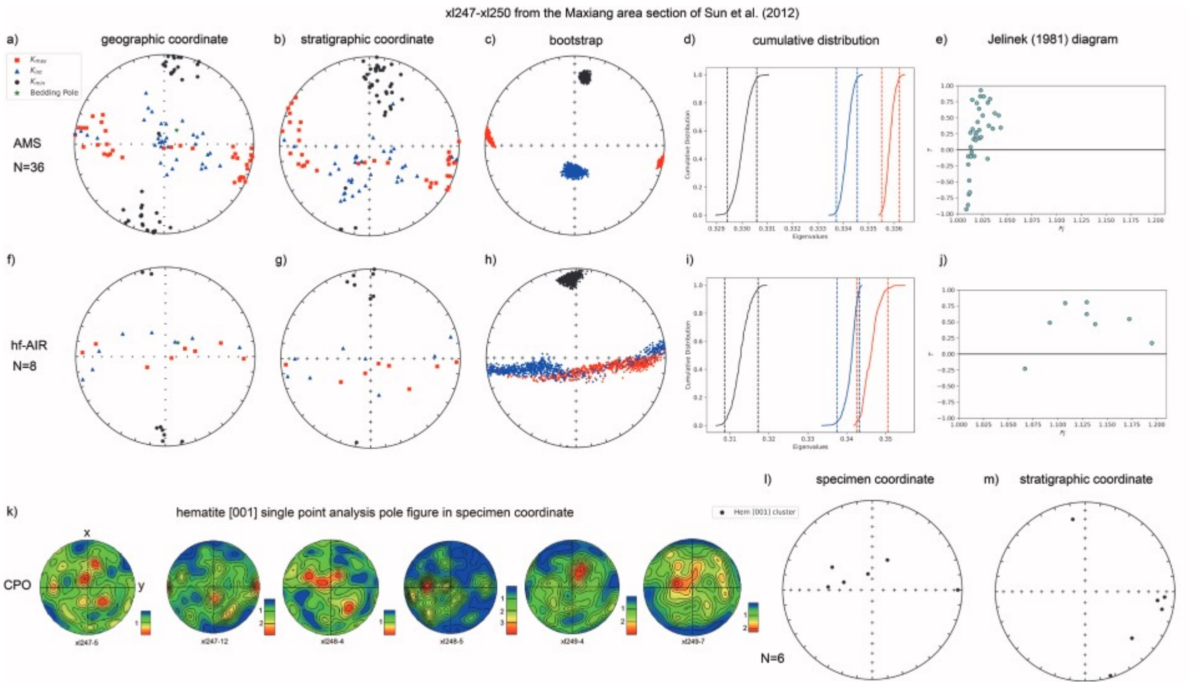

Figure 5. AMS, hf-AIR and CPO of hematite results of xl247-xl250 sites. (a-e) AMS results equal-area lower hemisphere projection in geographic coordinates and stratigraphic coordinates (with bootstrap results), the cumulative distribution of the bootstrap eigenvalues and Jelinek (1981) corrected anisotropy degree (Pj) versus ellipsoid shape factor (T) diagram (Pj-T). (f-j) hf-AIR results equal-area lower hemisphere projection in geographic coordinates and stratigraphic coordinates (with bootstrap results), the cumulative distribution of the bootstrap eigenvalues and Pj-T diagram. (k) Mapping pole figure of hematite [001] pole in equal-area lower hemisphere projection of specimen coordinates. (l and m) Equal-area lower hemisphere projection of the cluster directions of hematite [001] pole in specimen coordinates and stratigraphic coordinates.

The single point EBSD CPO data appeared dispersed (Figure 5k), akin to the findings for xl226-xl230 (Figure 4m), but certain samples revealed distinct, singular cluster orientations (Figure 5l). These clusters, when transformed into stratigraphic coordinates, aligned near the bedding plane (Figure 5m).

5 Discussion

5.1 Growth Strata Explanation in Tibet Plateau Paleomagnetic Study

Tong et al. (2019) used the concept of “syntectonic growth strata” to explain and “correct” the steeper ChRM inclinations observed in the southern limb of the anticline and the shallower inclinations in the northern limb from the Lhasa terrane. However, it is important to clarify that what they assumed is a syn-depositional tilt strata with syn-tilting magnetization, which differs from the classic concept of growth strata. Crucially, they didn’t offer any geological evidence for the existence of growth strata. To address this issue more accurately, we will refer to their assumption as "originally tilted strata" or "initially tilted strata" rather than "growth strata." While their approach was innovative, they unfortunately applied incorrect corrections to the paleomagnetic directions of these originally tilted strata.

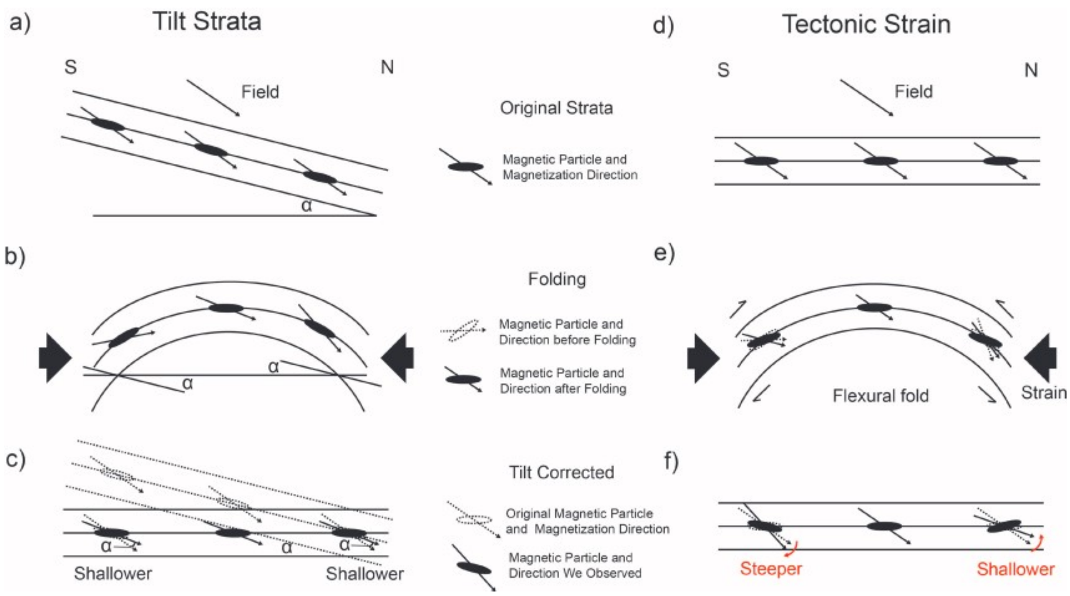

Figure 6. Schematic diagram of two models proposed to explain the inclination divergence of Late Cretaceous paleomagnetic data of the Lhasa terrane. (a-c) The growth strata model which cannot explain the phenomenon, see the detailed discussion in the text. (d-f) The tectonic strain model, which can potentially cause the inclination divergence.

Firstly, let's clarify what actually happens with the paleomagnetic inclination if the strata record a syn-tilting magnetization under Tong et al. (2019)'s assumption. Bedding planes form horizontally during deposition, but prior to the lock-in of magnetic particles and the recording of the magnetic field direction as ChRM, the strata undergo partial tilting due to tectonic activity (Figure 6a). During subsequent folding (Figure 6b), if tectonic strain does not rotate the hematite, the angle between the paleomagnetic direction and the bedding plane remains constant. When tilt correction is applied to both limbs without recognizing the original tilt (Figure 6c), the corrected inclinations on both limbs will appear shallower than expected if the strata were initially tilted northward. Conversely, if the strata were initially tilted southward, the corrected inclinations would appear steeper on both limbs. Regardless of the initial tilt direction, if the strata were straight and unbent at the time of magnetization, the tilt-corrected inclinations on both limbs should exhibit consistent variation rather than diverging.

Secondly, we explain why Tong et al. (2019) overlooked this simple principle and mistook the "syntectonic-sedimentation-correction" to "correct" the inclinations. In brief, we believe their error lies in mistaking strike + 180° instead of the actual strike to correct the original tilt strata in the south limb of the anticline. Next, we will outline the process through which we identified this error.

Table 1

Growth strata correction computation of the paleomagnetic data from Yang et al. (2015). **Dg** (**Ig**), **Strike**, **Dip** and **Ds** (**Is**) are paleomagnetic declination (inclination) in geographic coordinates, right-hand strike of bedding, dip angle of bedding and paleomagnetic declination (inclination) after normal tilt correction from Table 1 of Yang et al. (2015). **α** is the original dip of the syntectonic growth strata used in Table 3 of Tong et al. (2019) for Yang et al. (2015) paleomagnetic data. **Dc** and **Ic** are the paleomagnetic declination and inclination corrected from the **Ds** and **Is** with **Strike** and **α**. **Stike used** (= **Strike** + 180°**)** is the right-hand strike used for the correction of the south limb sites in Table 3 of Tong et al. (2019). **Dc used** and **Ic used** are the paleomagnetic declination and inclination corrected from the **Ds** and **Is** with **Strike used** and **α.**

South limb sites	**Dg (°)**	**Ig (°)**	**Strike (°)**	**Dip (°)**	**Ds (°)**	**Is (°)**	**α (°)**	**Dc (°)**	**Ic (°)**	**Strike used (°)**	**Dc used (°)**	**Ic used (°)**
CQ23	348.5	-2.7	113.0	48.0	339.1	35.5	14.2	330.0	44.9	293.0	344.5	24.8
CQ24	354.8	5.8	115.0	50.0	338.5	46.4	14.2	324.5	54.9	295.0	346.9	35.8
CQ25	347.3	6.6	112.0	53.0	327.3	46.2	14.2	312.4	52.9	292.0	336.9	37.0
CQ26	353.8	9.0	116.0	54.0	330.7	50.2	14.2	313.4	56.5	296.0	341.8	40.9
CQ27	352.9	8.1	123.0	52.0	332.1	43.1	14.2	318.5	48.6	303.0	341.8	35.1
CQ28	349.0	5.3	121.0	53.0	330.2	40.3	14.2	317.8	45.9	301.0	338.9	32.4
CQ29	356.2	4.0	119.0	53.0	338.7	45.4	14.2	324.7	53.1	299.0	347.5	35.4
CQ30	354.8	0.9	118.0	55.0	338.4	44.0	14.2	325.3	52.0	298.0	346.7	34.0
CQ31	340.9	15.6	43.0	33.0	351.4	43.6	14.2	2.8	53.8	223.0	345.1	31.9
CQ32	342.8	3.9	43.0	33.0	348.8	32.0	14.2	355.6	43.0	223.0	344.9	20.1
CQ33	335.1	-0.8	39.0	36.0	340.0	31.1	14.2	345.9	42.9	219.0	336.7	18.7
Mean (N=11)	**348.8**	**5.1**			**338.0**	**41.8**		**330.5**	**51.0**		**342.8**	**31.5**
Tong et al., 2019											**342.8**	**31.6**
North limb sites												
CQ1	275.3	34.0	277.5	64.0	308.1	15.9	-14.2	303.6	22.7			
CQ2	270.8	36.5	277.5	64.0	309.2	20.1	-14.2	303.8	27.1			
CQ3	267.1	40.8	277.0	66.0	313.1	22.6	-14.2	307.1	30.4			
CQ4	260.7	39.4	277.0	66.0	310.6	27.2	-14.2	303.2	34.3			

CQ5	262.4	37.2	277.0	66.0	308.5	25.4	-14.2	301.5	32.1
CQ6	260.8	33.5	273.0	65.0	300.6	23.2	-14.2	294.2	29.0
CQ7	271.3	34.9	278.0	64.0	308.1	19.7	-14.2	302.7	26.2
CQ8	274.8	37.1	278.0	63.0	311.0	18.3	-14.2	306.1	25.5
CQ9	267.4	42.8	278.0	61.0	314.2	26.6	-14.2	307.2	34.3
CQ10	265.8	36.4	278.0	59.0	306.1	26.9	-14.2	298.7	32.7
CQ11	264.3	40.2	278.0	63.0	311.6	27.0	-14.2	304.3	34.1
CQ12	269.3	35.0	280.0	62.0	308.4	23.8	-14.2	301.8	29.9
CQ13	265.0	25.3	277.0	60.0	294.3	22.1	-14.2	288.2	25.6
CQ14	262.6	33.0	273.0	63.0	299.8	22.5	-14.2	293.6	28.2
CQ15	263.9	34.5	273.0	63.0	301.7	21.9	-14.2	295.7	28.1
CQ16	261.9	38.1	279.0	62.0	309.1	29.6	-14.2	300.9	35.9
CQ17	267.6	35.1	279.0	62.0	307.3	24.3	-14.2	300.6	30.4
CQ18	271.0	32.1	274.0	62.5	302.0	16.5	-14.2	297.5	22.7
CQ19	263.8	33.3	277.0	61.0	301.7	24.9	-14.2	295.3	31.0
CQ20	258.9	29.1	274.0	65.0	296.2	24.3	-14.2	289.4	28.9
CQ21	295.9	63.6	277.0	51.0	338.8	26.8	-14.2	334.2	39.1
CQ22	300.4	52.5	267.5	44.0	324.6	20.0	-14.2	320.6	31.6
Mean (N=22)	**268.1**	**37.8**			**308.3**	**23.4**		**302.0**	**30.3**
Tong et al., 2019								**302.0**	**30.2**

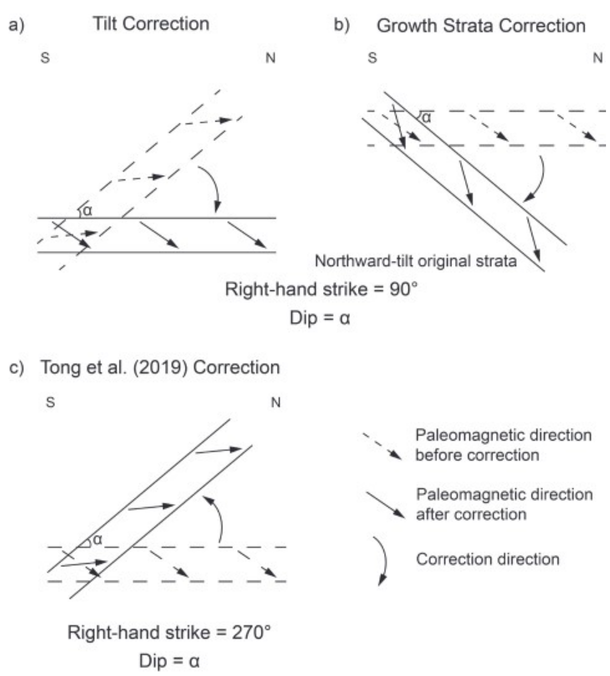

Figure 7. Schematic diagram of three bedding corrections. (a) Normal tilt correction from south limb strata to horizontal bedding. (b) Original tilt strata correction from horizontal bedding to northward-tilt original strata. (c) The erroneous correction made by Tong et al. (2019), which causes the inclination shallower.

In their description, firstly, they assumed an uncertain dip of a northward-tilting growth strata (defined as α, Fig. 7 in Tong et al., 2019 and Figure 6a here). With this α, you can correct the inclination from a horizontal bedding plane to an original tilt bedding (Figure 7b). They claimed that as the supposed α increases, the corrected inclination on the south limb decreases (Figure 7c) while that on the north limb increases. However, in reality, the inclination should increase (Figure 7b) on both limbs. Their counterintuitive results suggest erroneous original tilt strata corrections of the paleomagnetic directions. Tong et al. (2019) did not detail their computation process, so to pinpoint the error, we recalculated the original tilt strata correction (Table 1) using the paleomagnetic data from Yang et al. (2015), also referenced in Table 3 of Tong et al. (2019). Not surprisingly, while the calculated paleomagnetic declinations and inclinations after the growth strata correction from the north limb are consistent with those reported by Tong et al. (2019), the inclinations after correction from the south limb are higher than those reported by them (Table 1). When we applied a new right-hand strike = strike + 180° for the south limb (Table 1), we reproduced the mean value of declination and inclination reported by Tong et al. (2019). It can also be reproduced by applying the true strike and -α to conduct the correction. But according to their description of the strike they used (defined as "*C* + 180°"), we believe that the strike error, rather than the α error, is more possible. We understand that they used "*C* +180°" to represent "the right-hand strike of the originally northward-tilt strata". But if so, they should use -α as the dip, not α, because this clockwise correction of original tilt strata (Figure 7b) is the same as the normal tilt correction from the south fold limb to horizontal bedding (Figure 7a), and using "*C* +180°" and α will induce a counter-clockwise correction of southward-tilt strata (Fig. 7c).

To make it clear, using either *C* and α or *C* + 180° and -α yields the same and correct results for the south limb, but they used *C* + 180° and α, which leads to a decrease in inclination from the south limb as α increases, causing erroneous conclusions. Therefore, the inclination vs α graph (Fig. 8b in Tong et al., 2019) should never exhibit any intersection point between the two limbs. Therefore we cannot achieve a "corrected" mean direction for any further paleogeography reconstruction. Although likely unintentional, this significant error has already misled subsequent studies, including Bian et al. (2020), Wang et al. (2022) and Ma et al. (2023). In each of these works, the authors applied the "syntectonic-sedimentation-correction" method to their paleomagnetic data from two limbs.

In Zhao et al. (2021), a comment of Bian et al. (2020), they proposed a tectonic strain model to explain the discrepancies in magnetic inclinations between the two limbs. Here we demonstrate this model more directly in Figure 6d-6f. Initially horizontal strata record the magnetic field direction (Figure 6d) before undergoing tectonic strain. Then the formation of a flexural anticline fold leads to simple shear among beddings resulting in a clockwise rotation of remanence-carrying minerals in the south limb and a counterclockwise rotation in the north limb (Figure 6e, Kodama, 1988). Such differential rotations predictably steepen the magnetic inclination on the south limb while shallowing it on the north limb (Figure 6f), producing a "syn-folding" fold test result (Figure 1c).

In addition, Sun et al. (2023) used differences in the AMS fabric between sections at the growth end and in a stable depositional setting to identify growth strata in the Miocene strata of the Gengma Basin. Their conclusion relied on the observation that the inclination at the growth end is ~5° higher than in the stable depositional setting, while the average direction of K3 of the AMS fabric at the growth end deviates ~5° from the center of the equal-area projection. They suggested this deviation could act as an indicator and correction tool for detecting subtle growth strata. However, noting that the average direction of K3 from the stable deposition also deviates ~4° from the center (see Table S2 of their supporting information), we argue that the deviation of K3 from the pole of the bedding plane may not be a reliable marker for identifying growth strata.

5.2 Influence of Tectonic Strain on the Shexing Formation Redbeds

At the scale of block samples, no significant cleavage formation is observed in the Shexing Formation redbeds--otherwise, paleomagnetists would not invest time studying them. However, micromagnetic modeling by North et al. (2024) shows that the stress level required to alter (with alteration defined as a rotation >3°) the magnetization direction is only ~100 MPa, which is lower than the common stress in the formation of macroscopic cleavage in the absence of hydrothermal influence. It means the alteration of magnetic directions could come without visible macroscopic cleavage. This necessitates the use of alternative and indirect proxies, like magnetic fabrics, to assess the impact of tectonic strain on the redbeds minerals. Notably, the “cleavage fabric” found in magnetic fabric doesn’t indeed represent cleavage formation in weakly deformed rock (Parés, 2004).

AMS, containing the contributions from all paramagnetic, ferromagnetic and diamagnetic minerals, can be dominated by paramagnetic clay in the redbeds because of the relatively low susceptibility of hematite. This may result in a complex picture of AMS results for the Shexing Formation redbeds. The sedimentary or pencil structure fabric, as seen in samples xl226-xl230 of this study and in Cao et al. (2017) could be the case that undeformed clay minerals contribute mostly to the AMS. Other weak to strong cleavage in AMS, as in samples xl240-xl246 and xl247-xl250 here and in other studies (Liang et al., 2017; Ma et al., 2022), regardless of the proximity of sections, could be the case that deformed hematite dominates the AMS results. Moreover, completely contradictory AMS fabrics were obtained from the same section in this study (Figures 5a-5c) and Sun et al. (2012). If there was no artificial error, this may indicate that the AMS could be influenced significantly by the local abundance variation of the hematite in the same section.

On the other hand, hf-AIR, focusing on the high coecivity and high unblocking temperature ferromagnetic minerals, consistently shows deformed fabric across different sections, sometimes aligning with AMS (Figures 3b, 3g, 5b and 5g) and sometimes not (Figures 4b and 4h). Considering the west-east fold axis (Figure 2), the north-south *K*min distribution (Figures 3b, 3g, 5b and 5g) is consistent with the shortening direction of deformation and the rotation direction of the simple shear on the limbs of folds (Figure 6e). In addition, Hrouda et al. (2018) also described a decoupling between AMS and AMR in weakly deformed sedimentary rocks, where AMR foliation is more readily deflected away from the bedding plane, perpendicular to the maximum stress axis, than the AMS foliation. This suggests that ferrimagnetic minerals, which predominantly contribute to AMR, are more sensitive to ductile deformation than the paramagnetic clay minerals that dominate AMS. This might also apply to the Shexing Formation redbeds, where weak deformation is better recorded in hematite (Figure 4h) than in clay minerals (Figure 4b).

EBSD analysis further supports the notion of weak deformation in hematite. EBSD mapping shows the c-axis deflection of large detrital hematite towards the bedding plane (Figure 3m). However, single-point EBSD analysis reveals that the c-axis of all detrital hematite is not fully clustered (Figures 4o and 5m), as expected in those highly deformed rocks. The discrepancy between the orientation of *K*min in hf-AIR and CPO of the c-axis (Figures 3g, 3m, 4h, 4o, 5g and 5m) can also be explained by considering the presence of pigmentary hematite within the redbeds (Liang et al., 2017) which will influence the hf-AIR results (Bilardello, 2015).

In summary, the Shexing Formation redbeds have undergone a process of weak deformation, corroborated by the comparisons between AMS and hf-AIR and hematite CPO analysis via EBSD. This strain does not uniformly affect clay minerals across all studied regions or form macroscopic cleavage but does deflect hematite. Therefore, it is advised against using paleomagnetic data from the Shexing Formation redbeds for paleogeographic reconstructions without applying methodologies to correct this deflection.

5.3 Sufficient and Necessary Conditions for Reliable Paleomagnetic Data

The preceding discussion illustrates that sedimentary AMS fabric does not guarantee the reliability of paleomagnetic data, thus it is not a sufficient condition. Nor is it a necessary condition, as demonstrated by Jia et al. (2023) through their investigation of Mesozoic terrestrial sedimentary rock from the Nakhon Thai basin, Indochina Block. Even sites with strong cleavage fabric AMS in the Nam Phong and Phu Kradong formations, which would typically question paleomagnetic reliability, yielded ChRM directions consistent with other sedimentary fabric sites and neighboring basin results (Yan et al., 2017), passing the fold test. It strongly suggests that the ChRM captured at these sites is likely representative of the primary remanent magnetization.

On the other hand, sedimentary AMR fabric may be a better indicator of paleomagnetic data reliability. In the Shexing Formation redbeds, deformed hf-AIR fabric associated with the "syn-folding" ChRM suggests that sedimentary AMR fabric is possibly a necessary condition for paleomagnetic data without tectonic strain deformatiom. In the Nakhon Thai basin, sedimentary hf-AIR fabric in samples with strong cleavage AMS fabric (Jia et al., 2023), combined with primary remanent magnetization, indicates that sedimentary AMR fabric could be a sufficient condition for paleomagnetic data unaffected by tectonic strain. Therefore, it can be concluded that the sedimentary fabric of remanence-carrying ferromagnetic minerals might indeed represent both a sufficient and necessary condition for ensuring the primariness of paleomagnetic data.

However, we must acknowledge that the observed pattern of deformed AMS and sedimentary hf-AIR in the Nakhon Thai basin contradicts the explanation provided by Hrouda et al. (2018) that ferrimagnetic minerals are more sensitive to ductile deformation than paramagnetic clay minerals. This suggests that the interaction between ferrimagnetic and paramagnetic minerals under conditions of ductile deformation may be more complex than previously understood, necessitating further research to unravel these intricacies.

6 Conclusions

The ChRMs of the Upper Cretaceous redbeds from the Lhasa terrane consistently exhibit a pattern in which, after tilt correction, the inclinations on the southern limb of an anticline are steeper than those on the northern limb, resulting in a "syn-folding" fold test outcome (Bian et al., 2020; Liang et al., 2017; Ma et al., 2014; Sun et al., 2012; Tan et al., 2010; Tong et al., 2019; Yang et al., 2015). Tong et al. (2019) proposed a syntectonic sedimentation model to explain and correct for this inclination divergence. Unfortunately, their methodology rests on an error in converting the original horizontal strata to syntectonic tilt strata. With the analysis of AMS and hf-AIR fabrics and the CPO of hematite, we found that, regardless of the fabric displayed in the AMS data, the hf-AIR data from these redbeds demonstrate weak cleavage-deformational magnetic fabric, where the minimum axes correspond roughly with the c-axis of hematite in the bedding plane. Thus, we propose that the deflection of hematite due to weak deformation after sedimentation and compaction is possibly responsible for the observed inclination divergence. Therefore, we advise against using the Upper Cretaceous redbeds data from the Lhasa terrane for paleogeographic reconstruction, especially for paleo-latitude, without effective correction for tectonic strain. Additionally, by comparing results from the Shexing Formation with Mesozoic sedimentary rock from the Indochina Block (Jia et al., 2023), we suggest that AMR fabric, as a possible necessary and efficient indicator of tectonic unchanged remanence-carrying mineral, has better potential than AMS for assessing the primariness and reliability of paleomagnetic data in sedimentary rocks.

Acknowledgments

This research was funded by the National Natural Science Foundation of China (grant nos. 92055205 and 41774074). The authors declare that they have no known competing financial interests or personal relationships that could have appeared to influence the work reported in this paper. Lu expresses gratitude for the financial support received from the China Scholarship Council for sponsoring his visit to CENIEH.

Data Availability Statement

Supporting information and data set of AMS, hf-AIR and EBSD results is available at Lu et al. (2024).

References

Allegre, C. J., Courtillot, V., Tapponnier, P., Hirn, A., Mattauer, M., Coulon, C., Jaeger, J. J., Achache, J., Scharer, U., Marcoux, J., Burg, J. P., Girardeau, J., Armijo, R., Gariepy, C., Gopel, C., Li, T. D., Xiao, X. C., Chang, C. F., Li, G. Q., . . . Ronghua, X. (1984). Structure and Evolution of the Himalaya-Tibet Orogenic Belt. *Nature*, *307*(5946), 17-22. https://doi.org/10.1038/307017a0

Bian, W., & Yang, T. (2021). Reply to Comment by Zhao et al. on "Paleomagnetism of the Late Cretaceous Red Beds From the Far Western Lhasa Terrane: Inclination Discrepancy and Tectonic Implications". *Tectonics*, *40*(4), e2020TC006690. https://doi.org/10.1029/2020TC006690

Bian, W., Yang, T., Jiang, Z., Jin, J., Gao, F., Wang, S., Peng, W., Zhang, S., Wu, H., Li, H., Cao, L., & Deng, C. (2020). Paleomagnetism of the Late Cretaceous Red Beds From the Far Western Lhasa Terrane: Inclination Discrepancy and Tectonic Implications. *Tectonics*, *39*(8), e2020TC006280. https://doi.org/10.1029/2020tc006280

Biedermann, A. (2018). Magnetic Anisotropy in Single Crystals: A Review. *Geosciences*, *8*(8), 302. https://doi.org/10.3390/geosciences8080302

Bilardello, D. (2015). Isolating the anisotropy of the characteristic remanence-carrying hematite grains: a first multispecimen approach. *Geophysical Journal International*, *202*(2), 695-712. https://doi.org/10.1093/gji/ggv171

Bilardello, D., & Kodama, K. P. (2009). Measuring remanence anisotropy of hematite in red beds: anisotropy of high-field isothermal remanence magnetization (hf-AIR). *Geophysical Journal International*, *178*(3), 1260-1272. https://doi.org/10.1111/j.1365-246X.2009.04231.x

Cao, Y., Sun, Z., Li, H., Pei, J., Jiang, W., Xu, W., Zhao, L., Wang, L., Li, C., Ye, X., & Zhang, L. (2017). New Late

Cretaceous paleomagnetic data from volcanic rocks and red beds from the Lhasa terrane and its implications for the paleolatitude of the southern margin of Asia prior to the collision with India. *Gondwana Research*, *41*, 337-351. https://doi.org/10.1016/j.gr.2015.11.006

Dunlop, D. J., & Özdemir, Ö. (1997). *Rock Magnetism: Fundamentals and Frontiers*. Cambridge University Press. https://doi.org/10.1017/CBO9780511612794

Girdler, R. W. (1961). The Measurement and Computation of Anisotropy of Magnetic Susceptibility of Rocks. *Geophysical Journal International*, *5*(1), 34-44. https://doi.org/10.1111/j.1365-246X.1961.tb02927.x

He, S., Kapp, P., DeCelles, P. G., Gehrels, G. E., & Heizler, M. (2007). Cretaceous–Tertiary geology of the Gangdese Arc in the Linzhou area, southern Tibet. *Tectonophysics*, *433*(1-4), 15-37. https://doi.org/10.1016/j.tecto.2007.01.005

Hrouda, F., & Chadima, M. (2019). Examples of tectonic overprints of magnetic fabrics in rocks of the Bohemian Massif and Western Carpathians. *International Journal of Earth Sciences*, *109*(4), 1321-1336. https://doi.org/10.1007/s00531-019-01786-8

Hrouda, F., Gilder, S., Wack, M., & Ježek, J. (2018). Diverse response of paramagnetic and ferromagnetic minerals to deformation from Intra-Carpathian Palaeogene sedimentary rocks: Comparison of magnetic susceptibility and magnetic remanence anisotropies. *Journal of Structural Geology*, *113*, 217-224. https://doi.org/10.1016/j.jsg.2018.06.001

Jadoon, U. F., Zhao, Q., Huang, B., Yi, Z., Azeem, M. W., Lu, H., & Shah, S. A. (2024). A review of paleomagnetic constraints on the India-Asia collision: Paradoxes and perspectives. *Earth-Science Reviews*, *248*. https://doi.org/10.1016/j.earscirev.2023.104628

Jia, S., Huang, B., Lu, H., Zhao, Q., Yan, Y., Liang, Y., & Yi, Z. (2023). Reconnaissance on the constraint of rock magnetic fabrics on the reliability of remanent magnetization: A case study for Mesozoic detrital rocks from the Indochian Block and red beds from the Shexing Formation of the Linzhou Basin, Lhasa. *Chinese Journal of Geophysics (in Chinese)*, *66*(1), 301-313. https://doi.org/10.6038/cjg2022P0990

Kodama, K. P. (1988). Remanence rotation due to rock strain during folding and the stepwise application of the fold test. *Journal of Geophysical Research*, *93*(B4). https://doi.org/10.1029/JB093iB04p03357

Li, Z., Ding, L., Lippert, P. C., Song, P., Yue, Y., & van Hinsbergen, D. J. J. (2016). Paleomagnetic constraints on the Mesozoic drift of the Lhasa terrane (Tibet) from Gondwana to Eurasia. *Geology*, *44*(9), 727-730. https://doi.org/10.1130/G38030.1

Liang, Y., Huang, B., Yi, Z., Zhang, Y., Yan, Y., & Zhang, D. (2017). Reconnaissance of pre-collisional paleolatitudes of the southern margin of Eurasia:New paleomagnetic results from Upper Cretaceous red beds in the Linzhou basin,Tibet. *Chinese Journal of Geophysics*, *60*(5), 1811-1824. https://doi.org/10.6038/cjg20170517

Lu, H., Zhao, Q., Yi, Z., Huang, B., Parés, J. M. (2024). Supporting information for "Tectonic strain causes the inclination divergence of paleomagnetic data from the Upper Cretaceous redbeds in the Lhasa Terrane, insight from AMS, hf-AIR and CPO". Retrieved from https://figshare.com/s/8b3f0d0127c25da85c6f

Ma, J., Yang, T., Peng, W., Bian, W., Wang, S., Han, F., Liang, J., Jiao, X., Jin, J., Zhang, S., Wu, H., Li, H., & Ma, Y. (2023). New Late Cretaceous paleomagnetic and geochronologic results from the southern Qiangtang Terrane: Contributions to the reliability of redbed paleomagnetic datasets from the Tibetan Plateau and shape of the Qiangtang Terrane. *GSA Bulletin*, *136*(5-6), 1769-1786. https://doi.org/10.1130/b37023.1

Ma, Y., Wang, Q., Yang, T., Ou, Q., Zhang, X., Dan, W., Zhang, S., Wu, H., Li, H., Cao, L., Wang, J., Zou, D., & Wang, H. (2022). Location of the Lhasa terrane in the Late Cretaceous and its implications for crustal deformation. *Palaeogeography, Palaeoclimatology, Palaeoecology*, *588*, 110821. https://doi.org/10.1016/j.palaeo.2021.110821

Ma, Y., Yang, T., Bian, W., Jin, J., Wang, Q., Zhang, S., Wu, H., Li, H., Cao, L., Yuan, H., & Ding, J. (2017). Paleomagnetic and Geochronologic Results of Latest Cretaceous Lava Flows From the Lhasa Terrane and Their Tectonic Implications. *Journal of Geophysical Research: Solid Earth*, *122*(11), 8786-8809. https://doi.org/10.1002/2017jb014743

Ma, Y., Yang, T., Yang, Z., Zhang, S., Wu, H., Li, H., Li, H., Chen, W., Zhang, J., & Ding, J. (2014). Paleomagnetism and U-Pb zircon geochronology of Lower Cretaceous lava flows from the western Lhasa terrane: New constraints on the India-Asia collision process and intracontinental deformation within Asia. *Journal of Geophysical Research: Solid Earth*, *119*(10), 7404-7424. https://doi.org/10.1002/2014jb011362

Mo, X., Zhao, Z., Deng, J., Dong, G., Zhou, S., Guo, T., Zhang, S., & Wang, L. (2003). Response of volcanism to the India-Asia collision. *Earth Science Frontiers*, *10*, 135-148.

North, T. L., Muxworthy, A. R., Williams, W., Mitchell, T. M., Collins, G. S., & Davison, T. M. (2024). The Effect of Stress on Paleomagnetic Signals: A Micromagnetic Study of Magnetite's Single-Vortex Response. *Geophysical Research Letters*, *51*(2). https://doi.org/10.1029/2023gl106868

Parés, J. M. (2004). How deformed are weakly deformed mudrocks? Insights from magnetic anisotropy. *Geological Society, London, Special Publications*, *238*(1), 191-203. https://doi.org/10.1144/GSL.SP.2004.238.01.13

Parés, J. M. (2015). Sixty years of anisotropy of magnetic susceptibility in deformed sedimentary rocks. *Frontiers in Earth Science*, *3*. https://doi.org/10.3389/feart.2015.00004

Sun, X., Tong, Y., Yang, Z., Pei, J., Zhang, Z., & Hou, L. (2023). Identification of Growth Strata: New Insights From Anisotropy Corrected Paleomagnetic Data. *Geophysical Research Letters*, *50*(21). https://doi.org/10.1029/2023gl105625

Sun, Z., Pei, J., Li, H., Xu, W., Jiang, W., Zhu, Z., Wang, X., & Yang, Z. (2012). Palaeomagnetism of late Cretaceous sediments from southern Tibet: Evidence for the consistent palaeolatitudes of the southern margin of

Eurasia prior to the collision with India. *Gondwana Research*, *21*(1), 53-63. https://doi.org/10.1016/j.gr.2011.08.003

Tan, X., Gilder, S., Kodama, K. P., Jiang, W., Han, Y., Zhang, H., Xu, H., & Zhou, D. (2010). New paleomagnetic results from the Lhasa block: Revised estimation of latitudinal shortening across Tibet and implications for dating the India–Asia collision. *Earth and Planetary Science Letters*, *293*(3-4), 396-404. https://doi.org/10.1016/j.epsl.2010.03.013

Tapponnier, P., Mercier, J. L., Proust, F., Andrieux, J., Armijo, R., Bassoullet, J. P., Brunel, M., Burg, J. P., Colchen, M., Dupre, B., Girardeau, J., Marcoux, J., Mascle, G., Matte, P., Nicolas, A., Li, T. D., Xiao, X. C., Chang, C. F., Lin, P. Y., . . . Qiu, H. S. (1981). The Tibetan Side of the India-Eurasia Collision. *Nature*, *294*(5840), 405-410. https://doi.org/10.1038/294405a0

Tauxe, L., Shaar, R., Jonestrask, L., Swanson-Hysell, N. L., Minnett, R., Koppers, A. A. P., Constable, C. G., Jarboe, N., Gaastra, K., & Fairchild, L. (2016). PmagPy: Software package for paleomagnetic data analysis and a bridge to the Magnetics Information Consortium (MagIC) Database. *Geochemistry, Geophysics, Geosystems*, *17*(6), 2450-2463. https://doi.org/10.1002/2016gc006307

Tauxe, L., & Watson, G. S. (1994). The fold test: an eigen analysis approach. *Earth and Planetary Science Letters*, *122*(3), 331-341. https://doi.org/10.1016/0012-821X(94)90006-X

Tong, Y., Yang, Z., Li, J., Pei, J., & Li, J. (2019). New insights into the collision process of India and Eurasia: Evidence from the syntectonic-sedimentation-induced inclinational divergence of Cretaceous paleomagnetic data of the Lhasa Terrane. *Earth-Science Reviews*, *190*, 570-588. https://doi.org/10.1016/j.earscirev.2019.02.009

Tong, Y., Yang, Z., Pei, J., Wang, H., Xu, Y., & Pu, Z. (2017). Paleomagnetism of the Upper Cretaceous red-beds from the eastern edge of the Lhasa Terrane: New constraints on the onset of the India-Eurasia collision and latitudinal crustal shortening in southern Eurasia. *Gondwana Research*, *48*, 86-100. https://doi.org/10.1016/j.gr.2017.04.018

Wang, S., Yang, T., Gao, F., Bian, W., Jin, J., Peng, W., Jiao, X., Ma, J., Zhang, S., Wu, H., Li, H., & Cao, L. (2022). Paleomagnetic and geochronological results of the Risong Formation in the western Lhasa Terrane: Insights into the Lhasa-Qiangtang collision and stratal age. *Palaeogeography, Palaeoclimatology, Palaeoecology*, *586*. https://doi.org/10.1016/j.palaeo.2021.110778

Yan, Y., Huang, B., Zhao, J., Zhang, D., Liu, X., Charusiri, P., & Veeravinantanakul, A. (2017). Large southward motion and clockwise rotation of Indochina throughout the Mesozoic: Paleomagnetic and detrital zircon U–Pb geochronological constraints. *Earth and Planetary Science Letters*, *459*, 264-278. https://doi.org/10.1016/j.epsl.2016.11.035

Yang, T., Jin, J., Bian, W., Ma, Y., Gao, F., Peng, W., Ding, J., Wang, S., Zhang, S., Wu, H., Li, H., & Yang, Z. (2019). Precollisional Latitude of the Northern Tethyan Himalaya From the Paleocene Redbeds and Its

Implication for Greater India and the India-Asia collision. *Journal of Geophysical Research: Solid Earth*, *124*(11), 10777-10798. https://doi.org/10.1029/2019jb017927

Yang, T., Ma, Y., Zhang, S., Bian, W., Yang, Z., Wu, H., Li, H., Chen, W., & Ding, J. (2015). New insights into the India–Asia collision process from Cretaceous paleomagnetic and geochronologic results in the Lhasa terrane. *Gondwana Research*, *28*(2), 625-641. https://doi.org/10.1016/j.gr.2014.06.010

Yi, Z., Huang, B., Yang, L., Tang, X., Yan, Y., Qiao, Q., Zhao, J., & Chen, L. (2015). A quasi-linear structure of the southern margin of Eurasia prior to the India-Asia collision: First paleomagnetic constraints from Upper Cretaceous volcanic rocks near the western syntaxis of Tibet. *Tectonics*, *34*(7), 1431-1451. https://doi.org/10.1002/2014tc003571

Yin, A., & Harrison, T. M. (2000). Geologic Evolution of the Himalayan-Tibetan Orogen. *28*(1), 211-280. https://doi.org/10.1146/annurev.earth.28.1.211

Zhao, Q., Huang, B., & Tao, W. (2021). Comment on "Paleomagnetism of the Late Cretaceous Red Beds From the Far Western Lhasa Terrane: Inclination Discrepancy and Tectonic Implications" by Bian et al. *Tectonics*, *40*(4), e2020TC006520. https://doi.org/10.1029/2020TC006520

Journal of Geophysical Research: Solid Earth

Supporting Information for

Tectonic strain causes the inclination divergence of paleomagnetic data from the Upper Cretaceous redbeds in the Lhasa terrane, insight from AMS, hf-AIR and CPO

Hongliang Lu[1,2], Qian Zhao[3], Zhiyu Yi[4,5], Baochun Huang[1], and Josep M. Parés[2]

[1]Key Laboratory of Orogenic Belts and Crustal Evolution, School of Earth and Space Sciences, Peking University, Beijing 100871, China.

[2]Geochronology, Research Center for Human Evolution (CENIEH), Burgos 09002, Spain.

[3]Department of Resources and Environmental Sciences, Quanzhou Normal University, Quanzhou 362000, China.

[4]Planetary Environment and Astrobiological Research Laboratory (PEARL), School of Atmospheric Sciences, Sun Yat-sen University, Zhuhai, China.

[5]Key Laboratory of Tropical Atmosphere-Ocean System, Ministry of Education, Zhuhai 519082, China.

Contents of this file

Introduction

This document contains one figure, one table and one data set supporting the description and explanation in the main text.

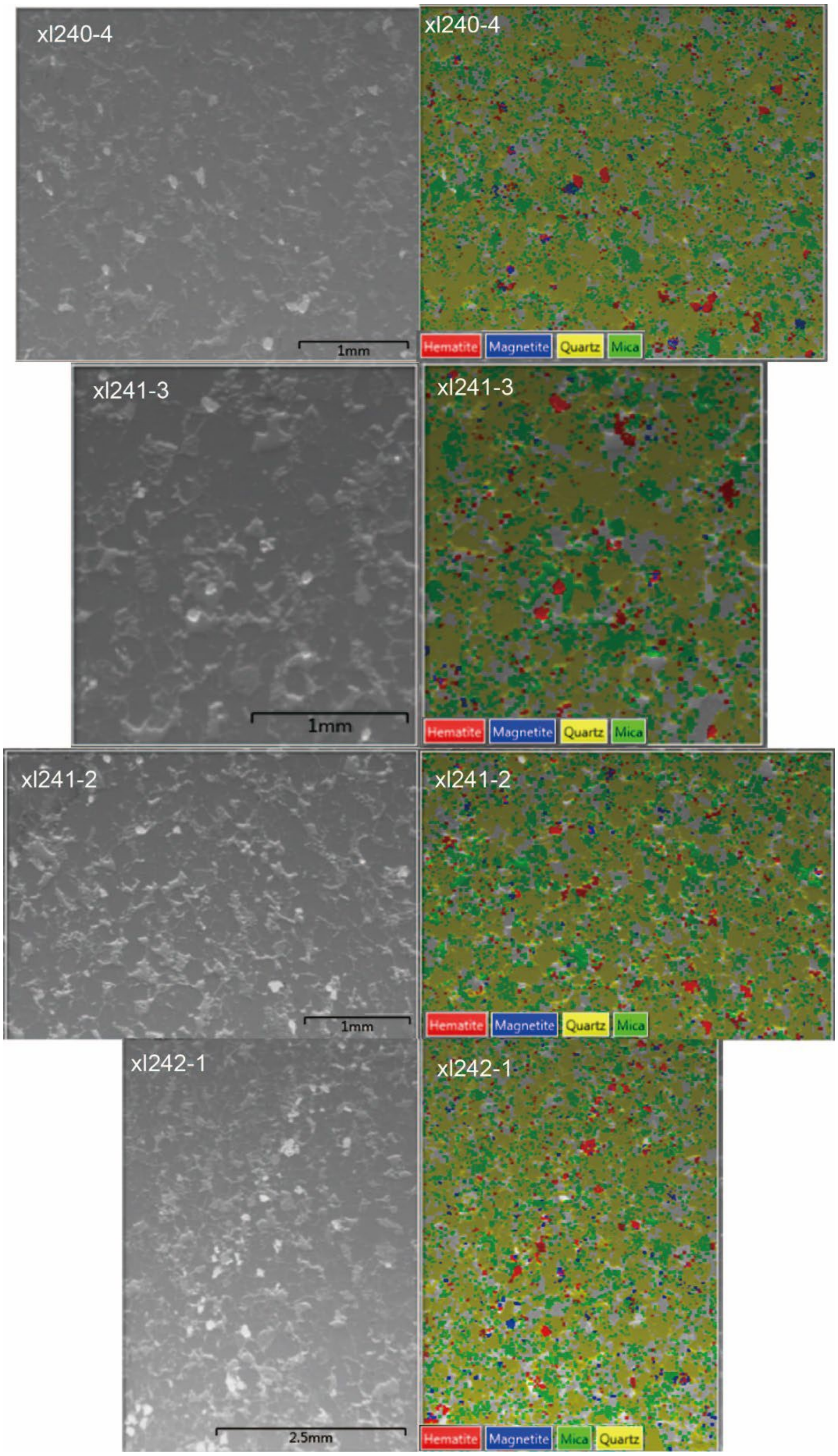

Figure S1. Secondary electrons microscope (SEM) photo (left) and mineral distribution (right) detected by electron backscatter diffraction (EBSD) of representative specimens.

Table S1. Field parameters of sampling sites. **n** is the number of samples per site. **Slat** (**Slong**) is the site latitude (longitude). **DD** is the dip direction of the bedding. **D** is the dip angle of the bedding.

Site	n	Slat (°N)	Slong (°E)	DD (°)	D (°)
Same section as section B in Tan et al. (2010) in Linzhou basin					
xl226	6	29.917744	91.270644	190	70
xl227	6	29.917744	91.270644	179	78
xl228	6	29.916946	91.272115	188	65
xl229	6	29.917194	91.272348	188	65
xl230	6	29.917194	91.272348	188	65
North limb of Shexing anticline					
xl240	6	29.903374	91.250824	336	36
xl241	7	29.903363	91.250774	319	29
xl242	7	29.903366	91.250748	317	21
xl243	9	29.903359	91.250702	320	27
xl244	7	29.903303	91.250602	320	27
xl245	7	29.903303	91.250602	325	44
xl246	8	29.903303	91.250602	325	44
Same section as Sun et al. (2012) in Maxiang area					
xl247	12	29.884858	90.726624	199	55
xl248	8	29.882338	90.727184	221	16
xl249	11	29.882260	90.727097	221	16
xl250	7	29.882260	90.727097	225	19

Data Set S1. The raw data of AMS, hf-AIR and EBSD results.